Micro-Precision Interferometer:
Pointing system solutions for on-orbit disturbance environment.

Frank G. Dekens, Greg Neat

Jet Propulsion Laboratory
California Institute of Technology
4800 Oak Grove Drive
Pasadena, CA 91109

ABSTRACT

We predict the contribution to the on-orbit residual tip-tilt performance due to the reaction wheel disturbance, for different isolator and closed loop optics configurations for the Space Interferometer Mission (SIM). SIM is required to point each arm of the interferometer to better than 0.07 micro-radian RMS residual jitter using a 0.01 Hz bandwidth optical sensor. We address the residual pointing error due to the the spinning spacecraft reaction wheel assemblies which emit disturbances from 2 Hz to 1 kHz. These estimates where obtained using the Micro-Precision Interferometer (MPI) testbed which is a dimensionally representative hardware model of a future space-borne optical interferometer. MPI is softly suspended and is therefore well suited to test in the frequency regime that the reaction wheels cause disturbances. The prediction of the on-orbit pointing error is determined in part by measuring broadband disturbance transfer functions from the testbed's isolated reaction wheel location to the camera output, where the pointing must be stabilized. Off-line, the procedure combines the measured testbed transfer functions with an empirical model of the reaction wheel disturbance to determine jitter over the entire range of wheel speeds. We present the results of both passive and active isolators and show that with an active isolator system, SIM will meet its requirement, due to the sensitivity of the optical system in the region the active isolator has improved isolation performance.

Keywords: space interferometry, isolation system, interferometry testbed

1. INTRODUCTION

Optical interferometers use an array of two or more telescopes in order to collect light from a single target star and obtain an improved resolution over the individual telescopes diffraction limit. The light from these telescopes, or sub-apertures, is combined to create an interference fringe pattern. Space Interferometer Mission (SIM) is a first-generation space-borne interferometer concept with astrometric and imaging goals.[1] The instrument will provide milli-arcsec imaging capabilities, micro-arcsec astrometric measurement capabilities and a technology demonstration of the nulling function. To achieve these goals, the cumulative displacements of the optical elements must be at the nanometer level and the beam pointing stability must be at the sub micro-radian (μrad) level. Unlike ground-based interferometers bolted to bedrock,[2] instrument optics of SIM will be distributed across a 10 m, light-weight flexible structure. In the presence of the primary mechanical disturbance source, the spinning reaction wheels, simulation results suggest that in the unattenuated spacecraft environment these stability requirements would be violated by as much as a factor of 1000.[3] This discrepancy inspired a layered vibration attenuation control strategy which involves the blending of vibration isolation, structural quieting, and active optical control. Evaluating such a strategy in a ground test environment implies the additional challenge of accurately representing the on-orbit disturbance conditions. To date, a number of testbeds have been designed, built and exercised to evaluate the progress on meeting the displacement or optical path-length difference requirement. We now addresses the status of meeting the pointing requirements.

Central to assessing the pointing performance is the Micro-Precision Interferometer (MPI) testbed .[4,5] Fig. 1 shows a bird's eye view of the MPI testbed. Located at the Jet Propulsion Laboratory, the testbed contains all the subsystems necessary to assess the effectiveness of the vibration attenuation technologies. These subsystems are: a

Further author information: (Send correspondence to F.G.D.)
F.G.D.: E-mail: fdekens@jpl.nasa.gov
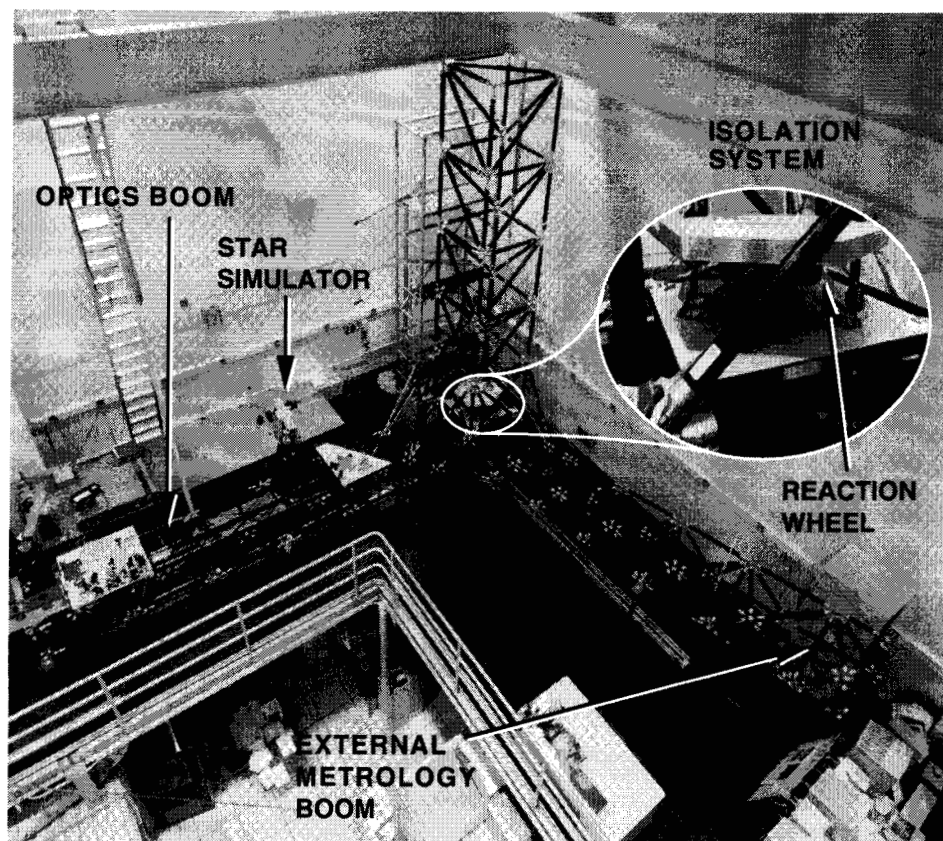G.N.: E-mail: neat@huey.jpl.nasa.gov

Figure 1. Bird's eye view of the MPI testbed with inset showing a close-up of a six-axis isolation system.

7 m x 7 m x 6.5 m softly suspended truss structure with mounting plates for subsystem hardware; a six-axis vibration isolation system which can support a reaction wheel assembly (RWA) to provide a flight-like input disturbance source; a complete Michelson interferometer; internal and external metrology systems; and a star simulator which provides stellar-like input to the interferometer collecting apertures.

Previous MPI studies[6,7] have assessed the severity of the on-orbit optical path difference (OPD) problem using an on-orbit prediction algorithm. The performance prediction procedure involves measuring disturbance transfer functions in six degrees of freedom from the reaction wheel attachment location to the output optical sensor. These transfer functions accurately depict (in a linear sense) how the disturbance propagates from the source to the optical detector. Modeled reaction wheel disturbance profiles are then played through this family of measurements to predict the on-orbit performance in terms of the desired optical metric. This same procedure is now used to predict the pointing error, as measured by a CCD camera, as a function of wheel speed.

We focus on the most challenging pointing problem, which is pointing the "science" interferometer. Each arm of this interferometer must be stabilized to 0.07 μrad root-mean-square[8] (RMS) while using a .01 Hz bandwidth sensor, which is effectively open loop. The only vibration attenuation strategy which can fight the reaction wheel disturbance at higher frequencies is the reaction wheel vibration isolation system. In addition to the open loop optics, isolated reaction wheel configuration, two other tests were performed to understand limitations of our measurement setup. One was a hard mounted ("no" isolator), open loop optic configuration which represents the maximum signal possible. The other case is the "perfect" isolator configuration, in which the disturbance is detached from the structure, and the pointing loop is closed using a fast steering mirror (FSM). This measurement provides the lower bound on our measurement or equivalently, tells us the measurement noise floor.

Sec. 2 presents the fundamentals of the pointing system for an interferometer and describes the specific MPI pointing system. In Sec. 3, we discuss how the MPI pointing problem relates to the SIM pointing problem. The product of this section is a pointing requirement which must be satisfied by the MPI system in order to prove the SIM system will meet its corresponding requirement.

The on-orbit prediction approach is described in Sec. 4. In Sec. 5, we discuss how the data is collected that is needed for the on-orbit pointing performance prediction and describe the different testbed configurations. The data along with the performance prediction metrics are presented in Sec. 6. This is done for three testbed configurations. Finally, we compare the performance predictions with the derived requirements to determine the status of the pointing problem.

2. POINTING SYSTEM DESCRIPTION

We will first briefly describe the MPI testbed. Fig. 2 is a schematic of the MPI optics boom and traces the optical path from the artificial star (on top in the figure) through the testbed's optical train. Everything inside of the
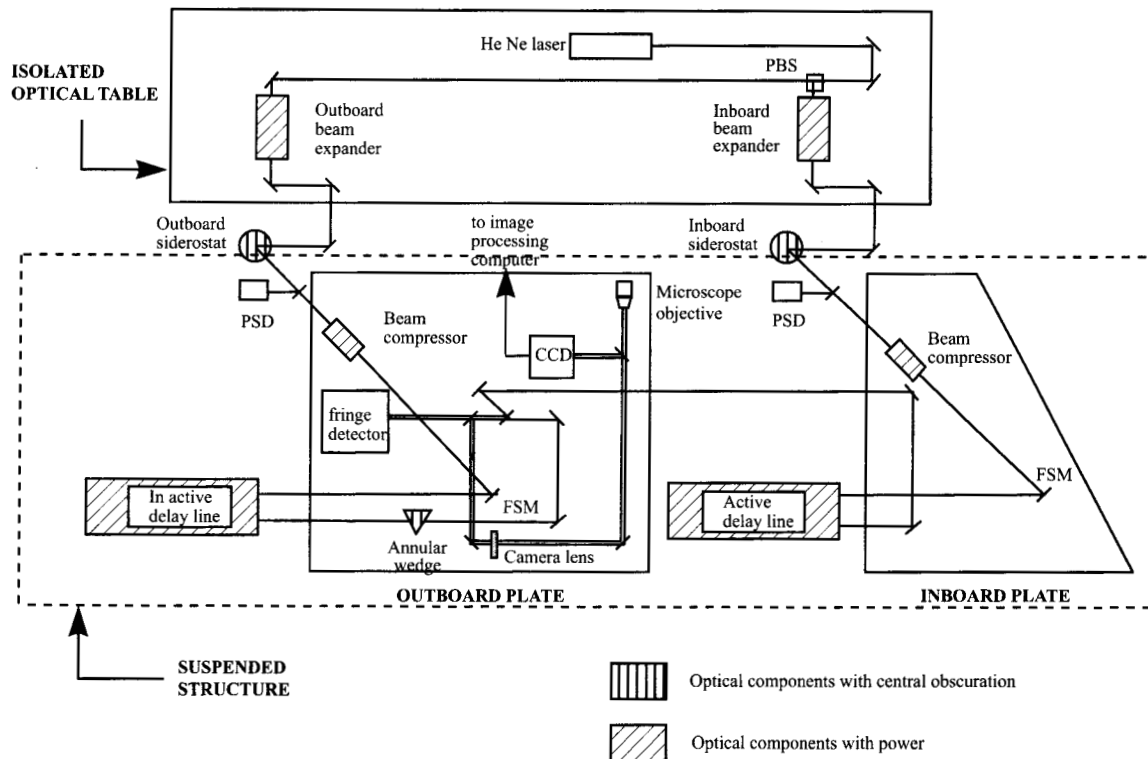

Figure 2. Optical layout of the Micro-Precision Interferometer.

dashed rectangle, including the siderostats, is on the suspended truss. The artificial star is a commercial heterodyne laser that sits on a pneumatically supported optical table. The beam is split by a polarizing beam-splitter (PBS) and each side is expanded to a 5 cm beam. A number of fold mirrors direct the beams to the two interferometer arms on the suspended MPI structure. The light path taken by the right-hand beam is described below, and the other path is similar. For the purposes of this paper, we only consider the right-hand side and will therefor describe its path. The left-hand path was blocked for all measurements described in this paper. The siderostat is the first optical element on the air-suspended structure. A subsequent beam compressor is used to reduce the input beam diameter from 5 cm to 3 cm to obtain an output beam suitable for traversing the delay line optics with sufficient light for the fringe-tracking sensor. Next comes a fast steering mirror (FSM) which is used for pointing control. Three piezo actuators position the mirror, providing tip and tilt motion for the closed-loop configuration, without introducing path length changes. After traveling through the active delay-line and a couple of folding mirrors, the inboard beam is reflected off of 50% beam splitter. Here the reflected light would join the transmitted beam from the left-handed path. After the beam combiner, the central portion of the combined stellar beams passes through the hole in an annular pick-off mirror to a fringe detector. The annular pick off mirror and subsequent folding mirrors reflect the outer annulus of each beam towards a high speed CCD camera. The 32 by 32 pixel Dalsa CCD camera is the sensor for the pointing control subsystem. The beam is focused by a 1 meter focal length lens, to a location on the CCD camera. A 5 by 5 pixel window is sampled at 4000 Hz, centered on the diffraction pattern location. The first moment

or position of the diffraction pattern is calculated, which we refer to as the centroid location. This is calculated as follows. Let I(i,j) be the intensity of the $(i,j)^{th}$ pixel in the CCD window. The offset from the center pixel is

$$\Delta x = \frac{\sum_{j=-isize}^{isize} \sum_{i=-isize}^{isize} iI(i+i_c, j+j_c)}{\sum_{j=-isize}^{isize} \sum_{i=-isize}^{isize} I(i+i_c, j+j_c)} \quad (1)$$

where *isize* is 2 for the 5 by 5 pixel case and (i_c, j_c) is the center pixel determined by the brightest pixel when the measurement is first begun. Thus the first image is used as a reference. The centroiding box is not moved. If a centroid moves outside of the range of the box during a measurement, the measurement is repeated. For subsequent frames, the offset from of the current centroid location to the reference centroid location is converted to two analog signals (the x and y offsets on the CCD coordinate system). The centroiding calculation is done in real time, at 4000 Hz, and the offsets are used as the output to a signal analyzer. There is a final calibration which is done, in order to compensate for a bias in the centroiding algorithm. This calibration factor is a function of box size and is 3.94 for a 5 pixel square box.

When we close the optics pointing loop, the centroiding signal is also fed to a loop algorithm, followed by two different digital to analog converters, which in turn drive the fast steering mirror. The details of the control loop are described by O'Brien.[9]

3. MAPPING MPI TO SIM

The current SIM design is on a 10 meter long flexible truss structure. The relevant baseline design parameters are shown in Table 1 along with the MPI requirements. The maximum allowable jitter on the MPI tip and tilt sensor

	SIM	MPI
Beam diameter	25 cm	3 cm
Compressor	11:1	1:1.5
Differential wavefront tip and tilt requirement	0.10 μrad	—
Single aperture wavefront tip and tilt requirement	0.07 μrad	—
Single aperture maximum tip and tilt on the detector	0.70 μrad	0.07 μrad

Table 1. SIM vs. MPI.

is such that if it is met, we have confidence that SIM will be able to obtain its pointing requirement on-orbit. The argument that MPI needs to meet the wave-front tilt requirements at the detector, despite the different optics and SIM's relaxed wave-front tilt requirements at the detector, goes as follows. What drives the requirement, is that the visibility reduction due to tip and tilt should be of order 1%. This implies a maximum RMS jitter between the two wavefronts from the different paths of the interferometer be less than 0.10 μrad. This is at the largest aperture size of 25 cm and a central wavelength of 0.55 μm. If the two arms have uncorrelated jitters, each arm is allowed 0.07 μrad of RMS tip and tilt errors. If we further assume the two directions, tip (x) and tilt (y), to also be independent, then each direction can have at most 0.05 μrad of RMS error.

Referring to Fig. 3, suppose that all optics on SIM are stationary, except for the siderostat of one arm, which is tilting by 0.10 μrad RMS along the y direction. As the light passes through the beam compressor, this angle in increased to 1.0 μrad at the 2.3 cm aperture. This means that SIM, at the detector, only needs to control or have less than 1.0 μrad RMS differential tip and tilt error. If instead of the siderostat a different optic is moving, which is past the compressor, it may move up to 1.0 μrad and still meet the required RMS tilt error because now the diameter has decrease by a factor of 11. Thus at the detector, SIM may see eleven times the required jitter and the most critical optical element is the siderostat, which is the only optical element that needs to be stationary (or compensated for) to 0.10 μrad. On MPI however, we do not have such a compressor (we will ignore the small compression ratio of 1:1.5 for this discussion). In order to guarantee that the siderostat does not move by more than 0.10 μrad, we need to stabilize the complete path to this level, since we can not distinguish which optics are moving. Thus MPI needs to have the wavefront tilt requirement of SIM at the MPI detector, not the wavefront at the SIM detector. MPI is therefore solving a slightly more difficult problem, in that MPI requires the combination of all the optics jitters to be less than 0.10 μrad, whereas SIM only needs the siderostat to be that stable. Care will have to be taken for the
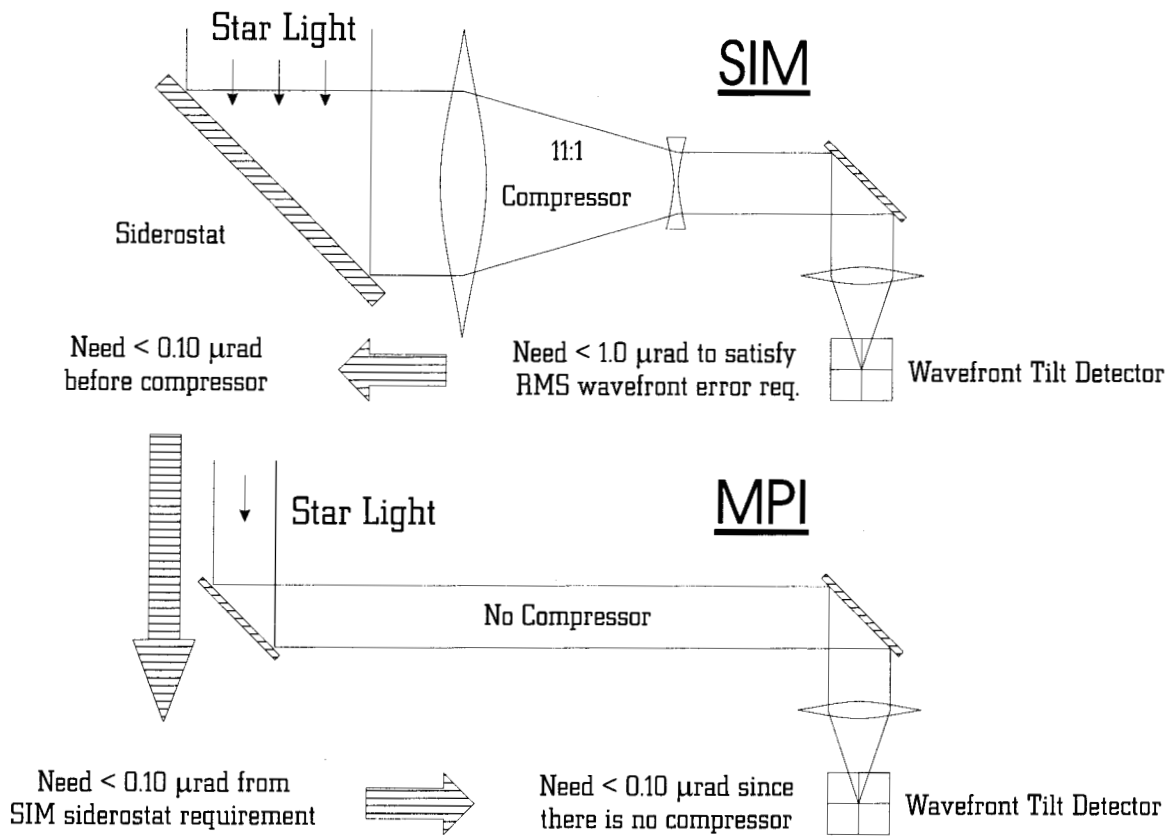
Figure 3. Comparison of optics and requirement of MPI verses SIM.

SIM sensor requirements, such that it can detect the centroid motion which is allowed to be 10 times larger, and the FSM will need to be able to control the larger motion. Note that neither of these are technical problems, just design considerations.

We have assumed that SIM will have a final beam size of 3 cm which is used for the angle measurement (which is similar to the MPI beam size), and that the F ratio and camera pixel size will be similar. Although we anticipate better reading noise in the camera used by SIM, we do not attempted to correct for this, which is more conservative.

4. PERFORMANCE PREDICTION PROCEDURE

The performance evaluation procedure combines disturbance transfer functions, measured from the testbed, with an analytical reaction wheel assembly (RWA) disturbance model. This method allows us to assess the pointing performance over an entire range of disturbance conditions that are expected during on-orbit observations. This hybrid experimental/analytical procedure predicts on-orbit performance in an accurate, efficient manner. Measuring performance solely in hardware would require measuring the optical metric while stepping through all combinations of wheel speeds for the four reaction wheel assemblies. The time required to perform this measurement is prohibitive. The test would also require having at least one reaction wheel and a suspension system to stabilize the testbed attitude in the presence of the spinning wheel. In addition, the time domain optical sensor data would be corrupted with ambient disturbances not traceable to space such as rigid body motion of the suspended structure, pseudo star motion, atmospheric effects on the laser beams, and acoustic disturbances from the ambient lab environment. Conversely, performing this assessment solely in analysis would require an accurate analytical representation (over all frequencies) of the structure, control system sensors and actuators and the disturbance sources. Attaining the necessary model fidelity is a challenge; especially at higher frequencies ($> 100 Hz$).[10] In addition, it is difficult to accurately represent the actuators and sensors, particularly with respect to practical implementation constraints such as noise floors and dynamic ranges.

Fig. 4 shows how the task of accurately representing the on-orbit problem has been distributed between the hardware and analysis tools. The four steps which make up this procedure are: (1) the analytical reaction wheel
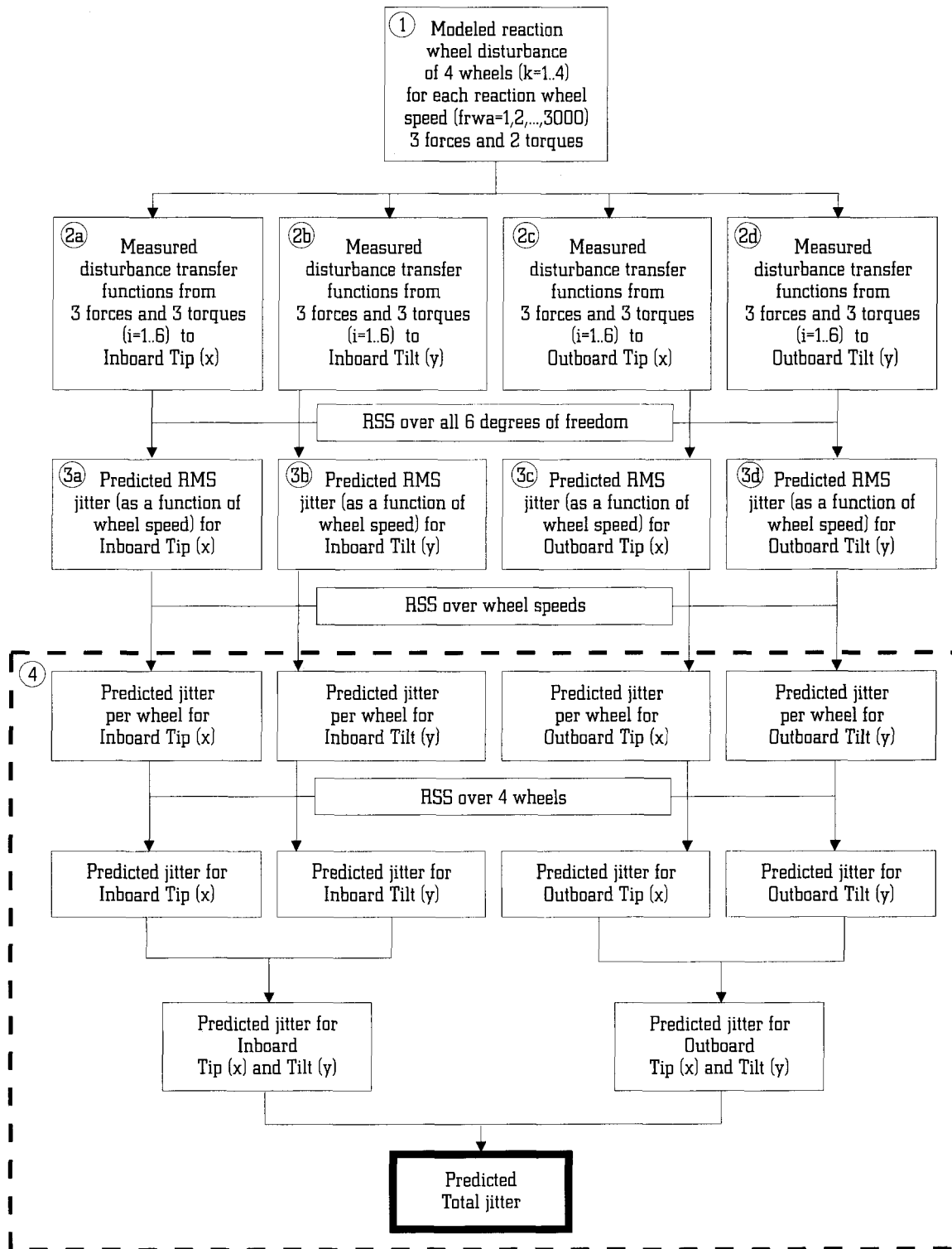

Figure 4. Data process to obtain on-orbit residual RMS tip/tilt error prediction.

disturbance model, (2) measured disturbance transfer functions, (3) the performance prediction algorithm yielding the

predicted RMS jitter as a function of wheel speed for each of the tips and tilts for the two arms of the interferometer, and (4) combining the data to a set of metrics which accurately predict the on-orbit jitter performance. These four steps are described in the following four sub-sections.

4.1. Reaction Wheel Model

Based on test data obtained from a HST flight reaction wheels,[11] the disturbance forces and torques are modeled as discrete harmonics of the reaction wheel speed, f_{rwa}, with amplitudes proportional to the wheel speed squared:

$$m(t) = \sum_{i=1}^{n} C_i f_{rwa}^2 \sin\left(2\pi h_i f_{rwa} t + \phi_i\right) \tag{2}$$

where $m(t)$ is the disturbance torque or force, C_i is an amplitude coefficient, h_i is the harmonic number, and ϕ_i is a random phase (uniform over $[0,\ 2\pi]$) used to account for phase uncertainty. According to this model, h_i and C_i uniquely determine the amplitude and frequency of each harmonic component for a given wheel speed. Melody et. al.[12] give the values for the different harmonics.

The disturbance model include one axial force (about the wheel spin axis), two radial forces (normal to the spin axis), and two radial torques (causing wheel wobble). These disturbances result from wheel imbalances and bearing imperfections.[11] Disturbance torque about the axis of rotation (from torque ripple or motor clogging) was found to be insignificant, and is therefor omitted.

The procedure requires reaction wheel disturbance power spectral densities (PSD) as input to the measured transfer functions. Given that the reaction wheel disturbances are sinusoidal wheel harmonics (Eq. 2), and assuming that the random phases (ϕ_i) are independent, identically-distributed,[8] the power spectral densities consist of Dirac delta functions[13] at the harmonic frequencies:

$$\Phi_m(\omega) = \sum_{i=1}^{n} \frac{\pi C_i^2 f_{rwa}^4}{4} \left[\delta\left(\omega - 2\pi h_i f_{rwa}\right) + \delta\left(\omega + 2\pi h_i f_{rwa}\right)\right] \tag{3}$$

where $\Phi_m(\omega)$ is the power spectral density of $m(t)$, and $\delta(t)$ is the Dirac delta function. As an example, Fig. 5 shows the power spectral density of axial force at a wheel speed of 1500 RPM. These PSDs are used as the start of the
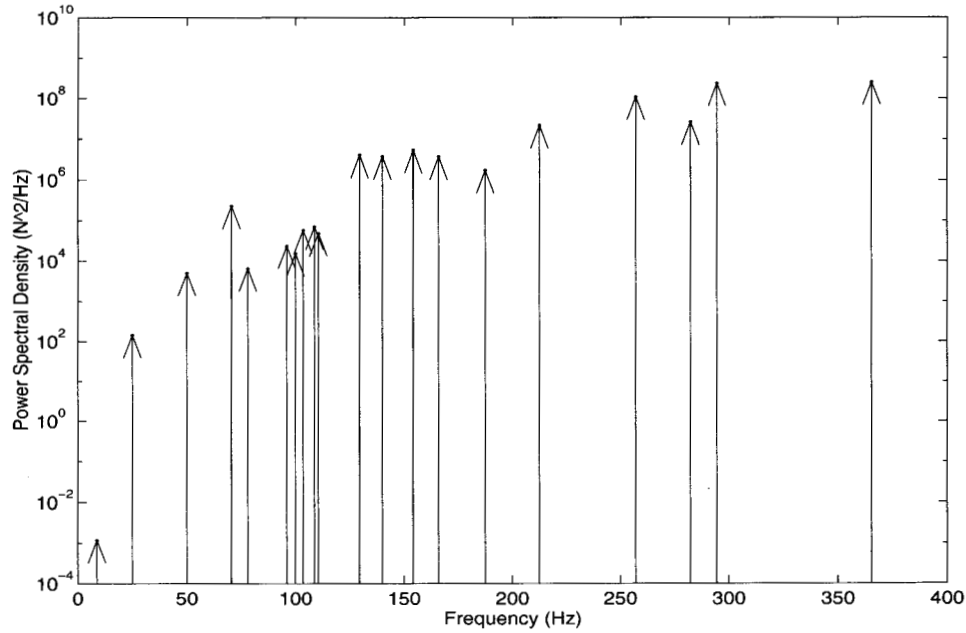

Figure 5. HST reaction wheel axial force disturbance PSD for a wheel spinning at 1500 RPM (Dirac delta function peaks are represented as arrows).

on-orbit prediction algorithm, i.e. the top box labeled 1 in Fig. 4.

4.2. Disturbance Transfer Function Measurements

The disturbance source consists of a pair of shakers mounted to a custom six-axis force measuring device (dynamometer). Fig. 6 shows the dynamometer with the two shakers. The dynamometer is mounted on the payload structure
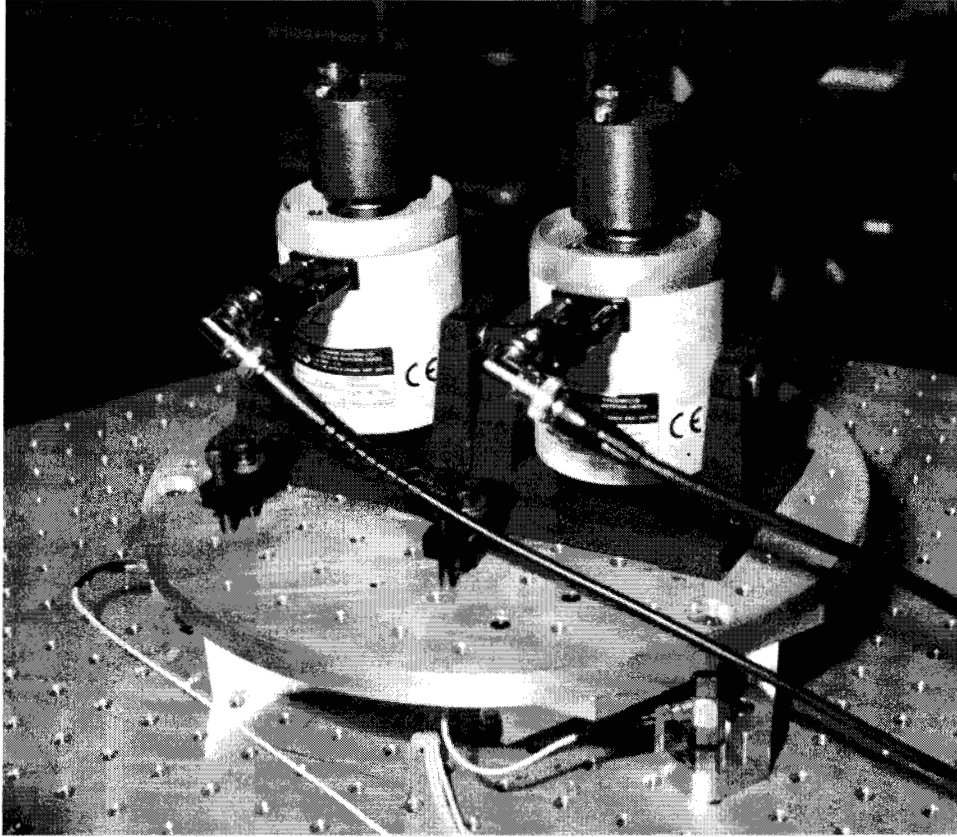

Figure 6. Dynamometer with two linear shakers on top producing a Z force shown on an optics bench. A load-cell between two flexure can be seen on the lower right of the picture.

and measures the forces and torques transmitted to the payload structure. The location of this can be seen in the inset of Fig. 1. Note that the hexagonal plate has been replaced by a triangular structure to decrease acoustical coupling which was occurring between the hexagonal plate and the plate below it, which is the mounting plate for the isolator and the disturbance source.

The dynamometer is a six degrees of freedom disturbance sensor. These six outputs are the three forces (X, Y and Z directions) and the three torques (along the X, Y and Z axis). The mechanical parts consist of the base plate, 6 load cells, 12 flexures and the top plate. The top plate is mounted to the base of the dynamometer only through the six load cells, three in the vertical direction and three in the horizontal one. The load cells are arranged in a triangular configuration. Two flexures are mounted on each side of the load cell to reduce the coupling between load cells. These flexures have to be soft enough the reduce the coupling but stiff enough so that the dynamometer modes are located above the frequency range of interest ($> 750Hz$).

Signal conditioning consist of the load cell signal amplifier and the analog transformation matrix board. This board converts the six signals from the six load cells into six outputs (X, Y, Z forces and X, Y, Z torques).

An HP signal analyzer is used to measure the disturbance transfer functions. The HP unit generates a broadband drive signal. This signal is sent to the two shakers through two power voltage amplifiers. To generate torques, polarity is inverted on one of the shakers. The bandwidth is divided into 3 ranges (2 - 14.5 Hz, 10 - 110 Hz and 100 - 900 Hz) with the driving voltage increasing with the frequency.

The dynamometer signal conditioner produces a voltage proportional to the disturbance. This voltage is sent to the HP analyzer as the input for the transfer function. The shakers are manually re-oriented to measure the six

different transfer functions. The output for the transfer functions are the tip and tilt offsets, which were described in Sec. 2.

4.3. Performance Prediction Algorithm

In the analysis, the on-orbit disturbance environment consists of four reaction wheels assemblies, as SIM is expected to carry a fourth RWA for redundancy. These wheels are assumed to be in a pyramidal configuration, i.e., the axis of each wheel is normal to a side of a square pyramid. The angle of the pyramid is taken to be 63°, since this yields equal torque capacity in all three spacecraft axes. Associated with each wheel orientation is a set of RWA local coordinates and a transformation from local to global coordinates. Applying this transformation to the disturbance transfer functions yields transfer functions from each RWA local disturbance direction to the inboard and outboard wave front tip or tilt. That is, from the twenty four global-coordinate transfer functions $H_n(\omega)$, eighty local transfer functions, $\tilde{H}_{jk}(\omega)$, were created. There are five disturbance directions per wheel (j-index) times four wheels (k-index) for tip and tilt on both the inboard and outboard arms. These eighty transfer functions are then the input to the disturbance model algorithm in order to determine wave front tip or tilt as a function of wheel speed.

The algorithm contains two nested loops with the outer loop indexing each wheel orientation (k=1-4) while the inner loop steps through all possible wheel speeds ($[f_{rwa}]_i$ = 1-3000 RPM). The kernel of the algorithm is the calculation of a wave front tip or tilt standard deviation, $[\sigma_{tip}]_{ik}$, for a single wheel speed (i-index) and orientation (k-index). For each wheel orientation, this calculation begins with five RWA disturbance PSDs generated from the wheel speed, f_{rwa} (an example RWA disturbance PSD is shown in Fig. 5). These PSDs, $[\Phi_m]_{ji}(\omega)$, are multiplied by the modulus squared of their corresponding local disturbance transfer functions, $\tilde{H}_{jk}(\omega)$, and summed to yield the wave front tip or tilt PSD, $[\Phi_{fp}]_{ik}(\omega)$:

$$[\Phi_{tip}]_{ik}(\omega) = \sum_{j=1}^{5} \left| \tilde{H}_{jk}(\omega) \right|^2 [\Phi_m]_{ji}(\omega) \qquad (4)$$

The cumulative area under the wave front tip PSD, $\left[\sigma_{tip}^2\right]_{ik}(\omega)$, is calculated by summing the PSD, $[\Phi_{tip}]_{ik}(\omega)$, over the measured range [2- 900 Hz]:

$$\left[\sigma_{tip}^2\right]_{ik}(\omega) = \frac{1}{\pi}\Delta\tilde{\omega} \sum_{\tilde{\omega}=2Hz}^{\omega} [\Phi_{tip}]_{ik}(\tilde{\omega}) \qquad (5)$$

When the integration limit approaches to total measured spectrum (up to 900 Hz), the cumulative PSD equals the variance, $\left[\sigma_{tip}^2\right]_{ik}$. The square root of this variance is the tip (or tilt) standard deviation, $[\sigma_{tip}]_{ik}$, for a given wheel speed and orientation. This value ($[\sigma_{tip}]_{ik}$) represents a single point in the plot of tip/tilt jitter as a function of wheel speed (RPM). This procedure produces four plots of σ_{tip} vs. f_{rwa}, one for each of the four wheel orientations. For a given plot, each point represents the standard deviation of a discrete-frequency power spectral density. It is not meaningful to combine these four plots into a single plot of σ_{tip} vs. a single wheel speed, since the four wheel speeds are generally not equal.

4.4. Metrics

The overall methodology uses two metrics for the pointing jitter performance: one which represents nominal operating conditions and one which represents worst case operating conditions. For each wheel, the worst-case metric, $[\sigma_{max}]_k$, is the maximum $[\sigma_{tip}]_k(f_{rwa})$ over the range of wheel speeds. The nominal metric, $[\sigma_{rss}]_k$, is the root-sum-square[8] of $[\sigma_{tip}]_k(f_{rwa})$ (RSS) over the wheel speed (i.e., the square root of the average variance)*. This is evaluated per wheel for each of the inboard and outboard tips and tilts. Both $[\sigma_{rss}]_k$ and $[\sigma_{max}]_k$ for each of the four wheel orientations are then root-sum-squared to assess the residual jitter of all four reaction wheels. This still produces four sets of metrics, tip and tilt for both the inboard and outboard side. The tip and tilt are then combined by taking the RSS of the two metrics. In the last step, the inboard and outboard metrics are again root-sum-squared to produce the final nominal and maximum predicted jitter performance.
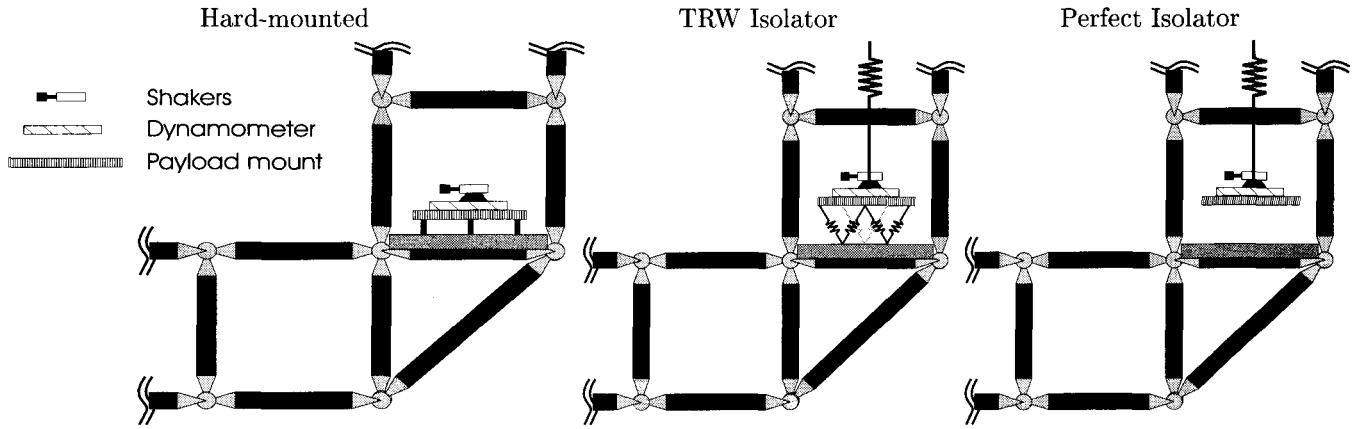
Figure 7. Three payload configurations.

5. TEST CONFIGURATIONS

In all testbed configurations, the shakers and dynamometer are mounted to a triangular payload plate. This presents our disturbance source. This combination replaces the hexagonal plate shown in the inset of Fig. 1. There are three different methods in which this is mounted to the testbed, as shown in Fig. 7. First is the hard-mounted case, where the disturbance source is mounted through three metallic posts to the base plate of the testbed and the optics are passive. This represents a worse case scenario. Next is a case where the disturbance source is placed on top of a 6-axis vibration isolation system made by TRW. This is a more probably configuration for SIM, for this disturbance will be isolated for all SIM operating modes. For the third configuration, the disturbance source is suspended by a bungee cord from the same I-beam that suspends the testbed and the optics loop is closed. This latter configuration no longer has a mechanical connection with the testbed. It therefor tests any electronic or acoustical coupling that may be present in the lab environment. The lack of coherence between our input disturbance and output centroid displacement indicates that there are no such flanking paths. This latter measurement is thus our measurement background noise. The same bungee cord which is used for the perfect isolator measurement is also used to offload the weight of the disturbance source when the TRW isolator is being used. This is because the isolator can not support the full weight of the disturbance source. Since there is no coherence in the perfect isolator case, we know that the bungee cord itself is not a flanking path when measuring the TRW isolator performance, and that indeed any difference between the TRW isolator measurement and the perfect isolator measurement is due to limitations of the TRW isolator.

6. RESULTS

A sample set of disturbance transfer functions are shown in Fig. 8. This is the response in the tip (x) direction on the camera when the testbed is disturbed along the y-direction at the disturbance source. The three curves represent the three different testbed configurations described in Sec. 5. There are a total of twelve different sets of transfer functions: a tip (x) and tilt (y) for each of the three force and three torque disturbances. Note that for now, we have only measured the inboard (or right hand) arm transfer function.

Once a set of twelve transfer functions are measured for a particular configuration, we process the data to predict the on-orbit RMS jitter through the previously described method (Sec. 4), where the transfer functions are represented by the boxes 2a-2d in Fig. 4.

The next step in the algorithm is to calculate the predicted RMS jitter as a function of wheel speed. There are eight such plots: tip and tilt for each of the four reaction wheel assemblies. Fig. 9 shows an example of such a plot for the case of tip (x), in μradians, versus wheel speed, in RPM, for wheel xxx. Again the three curves represent the three testbed configurations. These curves are represented by the boxes 3a-3d in Fig. 4.

---

*The justification for these metrics are given by Neat[6] and references therein.
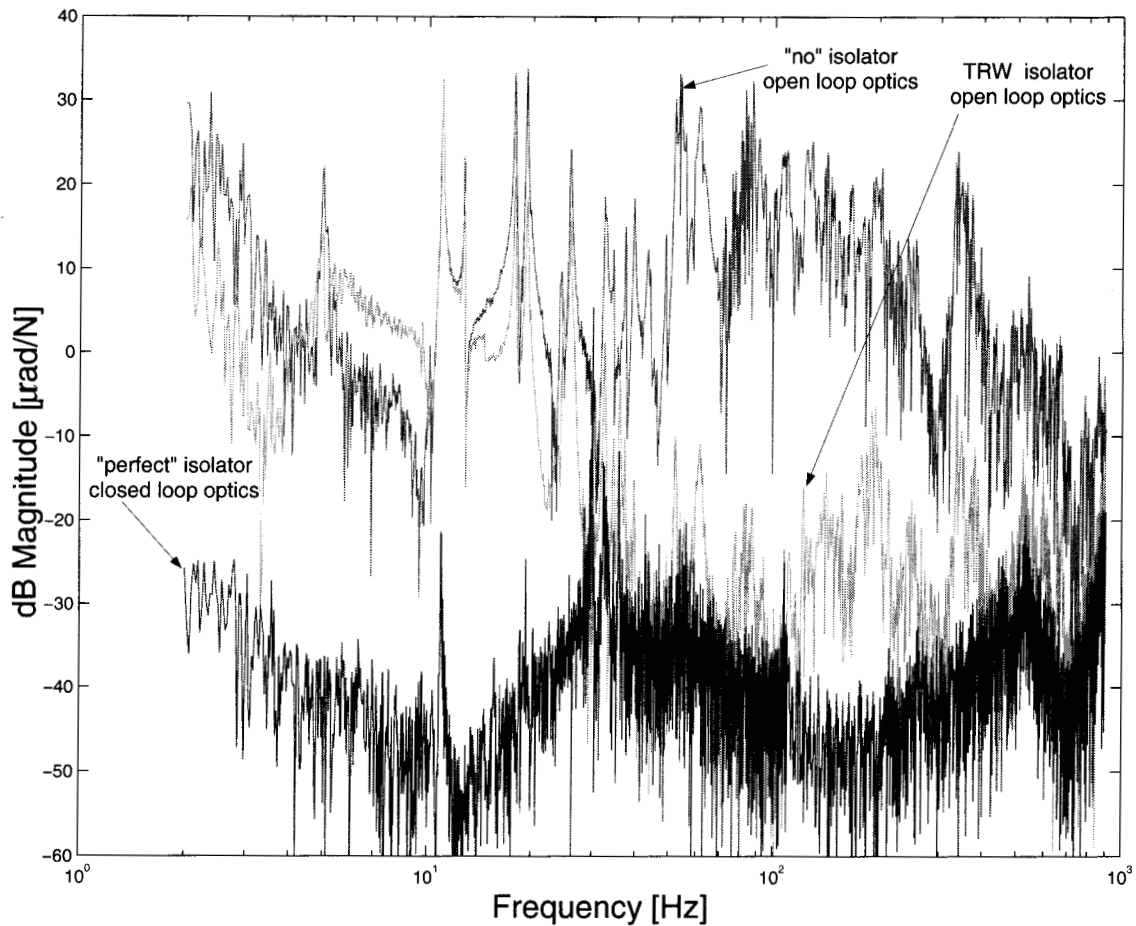
Figure 8. Comparison of the tilt wavefront tip (x) error while introducing a Y-force disturbance on the tested under different isolator and optics conditions.

Each curve is now collapsed over the reaction wheel speed into a set of eight metrics indicative of the tip and tilt jitters from a single reaction wheel. The two methods for this were described in Sec. 4.4 and yield the nominal and maximum jitter per reaction wheel. These values are summarized in Table 2.

The results of the four wheels are subsequently added in quadrature to form a predicted total RMS jitter for tip and tilt. These are the top two rows of Table 3. For reference, the associated SIM requirements are given in the last column. The table next shows the tip and tilt jitters again added in quadrature to give the total RMS jitter per interferometer arm. Finally, since the jitter in the second arm has not been measured yet, the latter value is multiplied by the square root of two to predict the differential jitter between the two interferometer arms. This is the fourth row of Table 3. The same calculation if performed for the maximum metric, which is given in the second half of the table.

7. DISCUSSION AND FUTURE WORK

Figure Fig. 9 succinctly summarizes the results of this study. For the most challenging astrometric pointing problem, the predictions suggest the jitter is above the requirement by a factor of 10 (compare the TRW isolator, open loop optics curve with the requirement). In addition, the predictions suggest that we have a low enough noise floor
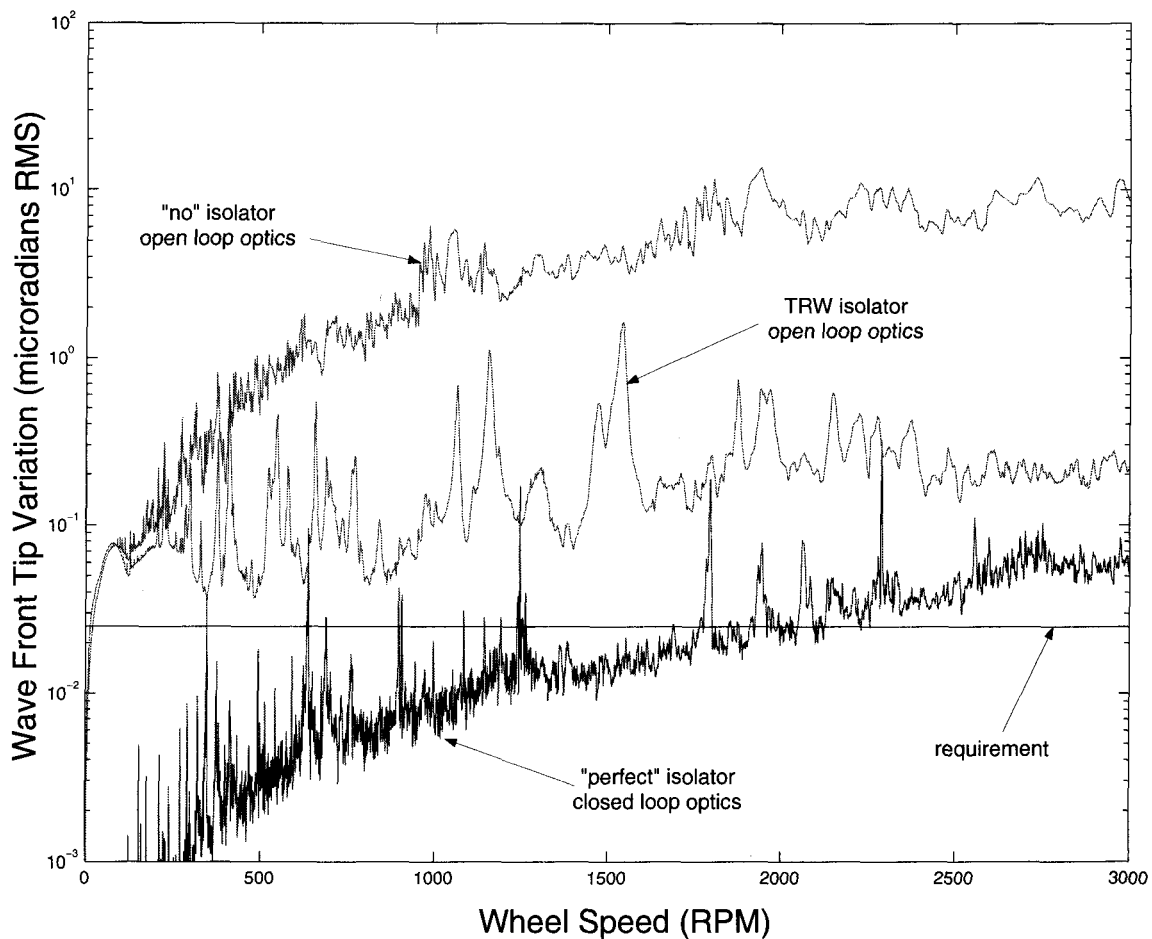
**"no" isolator
open loop optics**

**TRW isolator
open loop optics**

**"perfect" isolator
closed loop optics**

requirement

Wave Front Tip Variation (microradians RMS)

10^2 10^1 10^0 10^{-1} 10^{-2} 10^{-3}

0   500   1000   1500   2000   2500   3000

Wheel Speed (RPM)

Figure 9. Predicted on-orbit wavefront tilt jitter verses reaction wheel speed for four configurations. The horizontal line is the corresponding SIM requirement.

to demonstrate the most challenging requirement, except for a region at high reaction wheel speeds (compare the "perfect" isolator, closed loop optics curve with the requirement).

A number of short and long term future activities fall out of this work. In the near term, we will measure the outboard disturbance transfer functions and apply the complete prediction algorithm as described in Sec. 4. Thus far, we only measured the inboard pointing system jitter and assumed it would be the same for the outboard. We will also measure the open loop optics with a number of other isolator configurations. In addition to the hard mounted ("no" isolator) and TRW isolator considered in this study, the elastomeric isolator[6] and the "perfect" isolator are of interest. These would potentially improve on the present factor of 10 requirement discrepancy and provide a lower limit on the measurement noise floor respectively. Based on our experience with the optical path difference measurements, we conjecture that isolator improvements will narrow the requirement gap by at least a factor of 2. The remaining improvement must come from the closed loop optical system.

In the longer term, we will apply the performance prediction algorithm to the closed loop optics, isolated disturbance configuration. With an optical bandwidth of 100 Hz, this setup will address the SIM "guide" interferometer pointing problem, which observes bright target stars. Worst case, the optical system must provide a factor of 10 for this configuration to meet the requirement. For the science interferometer pointing system, the remaining error may need to be addressed by some other system. One concept under consideration by the SIM design team is to provide

	Hard-mounted open loop [μrad]	TRW isolator open loop [μrad]	Perfect isolator closed loop [μrad]
Nominal Tip (x)			
RWA # 1	5.7721	0.2667	0.0331
RWA # 2	5.9455	0.2679	0.0331
RWA # 3	5.4490	0.2514	0.0339
RWA # 4	5.6815	0.2510	0.0343
Nominal Tilt (y)			
RWA # 1	6.7847	0.4393	0.0299
RWA # 2	7.1944	0.4417	0.0299
RWA # 3	7.0487	0.4354	0.0323
RWA # 4	7.4663	0.4275	0.0323
Maximum Tip (x)			
RWA # 1	13.5654	1.6572	0.3215
RWA # 2	13.4433	1.6052	0.2987
RWA # 3	13.4157	1.2742	0.2202
RWA # 4	13.8255	1.2234	0.2549
Maximum Tilt (y)			
RWA # 1	17.2651	1.9960	0.1013
RWA # 2	17.6630	2.0240	0.1040
RWA # 3	20.2713	1.9204	0.1403
RWA # 4	21.6897	1.8057	0.1458

Table 2. Predicted tip and tilt nominal and maximum jitters per reaction wheel assembly for three testbed configuration.

	Hard-mounted open loop [μrad]	TRW isolator open loop [μrad]	Perfect isolator closed loop [μrad]	SIM requirement [μrad]
Nominal Inboard RMS Tip (x) jitter	11.430	0.518	0.067	0.050
Nominal Inboard RMS Tilt (y) jitter	14.250	0.871	0.062	0.050
Nominal Inboard RMS total jitter	18.270	1.014	0.091	0.071
Nominal Total RMS jitter	25.840	1.435	0.129	0.100
Maximum Inboard RMS Tip (x) jitter	24.190	2.905	0.518	0.050
Maximum Inboard RMS Tilt (y) jitter	37.380	3.877	0.228	0.050
Maximum Inboard RMS total jitter	44.520	4.844	0.566	0.071
Maximum Total RMS jitter	62.960	6.851	0.801	0.100

Table 3. Predicted tip/tilt jitter versus configuration.

a beacon and separate tip/tilt sensor, which measures internal tips and tilts of each interferometer arm for high frequencies compared to the integration time on the star. This would become a feedback signal for the pointing system actuators in the respective interferometer arms. This "internal" tip-tilt control system must provide the disturbance rejection to achieve the requirement (worst case, a factor of 10). One final possibility for improvement, would be to use different, more quiet, reaction wheel assemblies for SIM. However, this must be a design issue considered at the SIM system level.

8. CONCLUSION

A method of predicting on-orbit residual jitter has been presented which expands upon the already established on-orbit path length difference prediction algorithm. Results suggest that the pointing jitter requirement is violated by a factor of 10 for the most challenging instrument configuration: science interferometer in observing mode. In addition,

results suggest that the lab noise floor is low enough to measure the science interferometer pointing performance at the requirement level. We suggest a number of future activities that focus on narrowing the requirement gap. These include: test different isolators, including elastomeric cubes which have proven to work well for the OPD case; reduce the background noise in the MPI lab environment; design and build a method by which internal high frequency tip/tilt jitter can be measured independent from the star light.

ACKNOWLEDGMENTS

REFERENCES

1. M. Shao and D. M. Wolf, "Orbiting stellar interferometer," in Reasenberg,[14] pp. 228–239.
2. M. Shao, M. M. Colavita, B. E. Hines, D. H. Staelin, D. J. Hutter, K. J. Johnston, D. Mozurkewich, R. S. Simon, J. L. Hersey, J. A. Hughes, and G. H. Kaplan, "Mark III stellar interferometer," *Journal of Astronomy and Astrophysics* **193**, pp. 357–371, 1988.
3. R. A. Laskin and M. S. Martin, "Control/structure system design of a spaceborne optical interferometer," in *AAS/AIAA Astrodynamics Specialist Conference*, (Stowe, VT), Aug. 1989.
4. G. W. Neat, J. F. O'Brien, N. M. Nerheim, R. J. Calvet, H. Singh, and S. Shaklan, "Micro-precision interferometer testbed: First stabilized stellar fringes," in Reasenberg,[14] pp. 104–115.
5. G. W. Neat, A. Abramovici, J. W. Melody, R. J. Calvet, N. M. Nerheim, and J. F. O'Brien, "Control technology readiness for spaceborne optical interferometer missions," in *Proc. Space Microdynamics and Accurate Control Symposium*, (Toulouse, France), May 1997.
6. J. F. O'Brien, R. Goullioud, and G. W. Neat, "Micro-precision interferometer: Evaluation of new disturbance isolation solutions," in *Proceedings of SPIE's 6th Annual International Symposium on Smart Structures and Materials*, (San Diego, CA), Mar. 1997.
7. G. W. Neat, A. R. Abramovici, R. J. Calvet, R. P. Korechoff, S. S. Joshi, and R. Goullioud, "Use of the microprecision interferometer testbed for developing control technology for spaceborne optical interferometer missions," in *Astronomical Interferometry*, R. D. Reasenberg, ed., vol. 3350, pp. 1020–1030, SPIE, July 1998.
8. A. Papoulis, *Probability, Random Variables, and Stochastic Processes*, McGraw-Hill, New York, 3rd ed., 1991.
9. J. F. O'Brien and G. W. Neat, "Micro-precision interferometer: Pointing control system," in *Conference on Control Applications*, vol. 4, CCA, 1995.
10. J. W. Melody and G. W. Neat, "Integrated modeling methodology validation using the micro-precision interferometer testbed," in *Proc. 35th IEEE Conference on Decision and Control*, vol. 4, pp. 4222–4227, (Kobe, Japan), Dec. 1996.
11. M. D. Hasha, "Reaction wheel mechanical noise variations," Engineering Memorandum SSS 218, LMSC, June 1986.
12. J. W. Melody, "Discrete-frequency and broadband reaction wheel disturbance models," Interoffice Memorandum 3411–95–200csi, JPL, June 1995.
13. C. H. Edwards and D. E. Penny, *Elementary Differential Equations*, Prentice-Hall, Inc., Englewood Cliffs, NJ, 1985.
14. R. D. Reasenberg, ed., vol. 2447 of *Proc. SPIE*, (Orlando, FA), Apr. 1995.